Competitive binding strategy for reliable signal-off surface enhanced Raman scattering sensing in protecting apples from patulin without external interference

Yang Zhang [a], Xinchen Wu [a], Limei Yin [a], Pierre Picchetti [b], Tianxi Yang [c], Ruiyun Zhou [a], Chuping Zhao [a], Shanshan Xue [a], Zhepeng Zhang [a], Xiaobo Zou [a], Zhiming Guo [a,*]

[a] China Light Industry Key Laboratory of Food Intelligent Detection & Processing, International Joint Research Laboratory of Intelligent Agriculture and Agri-products Processing, Jiangsu University, Zhenjiang 212013, China
[b] Institute of Nanotechnology (INT), Karlsruhe Institute of Technology (KIT), Kaiserstrasse 12, Karlsruhe 76131, Germany
[c] Food, Nutrition and Health, Faculty of Land and Food Systems, The University of British Columbia, Vancouver, BC V6T 1Z4, Canada

Keywords:
Patulin
Surface enhanced Raman scattering
Core-Raman molecule-shell nanostructure
Metal-organic frameworks

A B S T R A C T

Patulin is a toxin that can be found in damaged or moldy fruits, especially apples. Very high detection sensitivity can be achieved using the SERS (Surface Enhanced Raman Scattering) technique, which provides information about molecular vibrations. However, unexpected desorption of target toxins from the surface of the SERS substrate and interference from other substances pose a major challenge. Here we investigate a competitive binding strategy for reliable SERS analysis of PAT. Core-Raman molecule-shell (CMS) structures and programmable, specific DNA interactions are utilized to regulate Raman signal intensity without affecting the embedded Raman molecules. Specfically, aptamer-functionalized CMS structures are combined with metal-organic scaffold nanoparticles that possess complementary DNA sequences. In the presence of PAT, binding of the aptamer to the toxin leads to degradation of the hybrid nano assembly, which can be measured by a change in the SERS signal. This SERS strategy enables turn-off sensing in apple juice over a wide range (10 pg/mL to 1 μg/mL), with a detection limit as low as 0.02 ng/mL. Analysis of real samples gives results consistent with high-performance liquid chromatography (HPLC) test. The excellent selectivity and sensitivity of the SERS sensor demonstrate its potential for a wide range of SERS sensor applications.

1. Introduction

Contamination with mycotoxins is a global challenge for ensuring food safety (Kabak et al., 2006). Ingestion of food-borne mycotoxins can cause acute symptoms of serious illness or long-term health effects, typically leading to cancer and immune deficiencies (Haque et al., 2020). Patulin (PAT) is a mycotoxin commonly found in contaminated apples and apple products, but it also exists in moldy pears, apricots, tomatoes, figs, cheese and grains like corn, rice, and wheat, etc. (Mahato et al., 2021). Consumption of contaminated food can lead to acute symptoms, including vomiting and gastrointestinal disturbances, while chronic exposure has been linked to immunotoxicity, mutagenicity, and genotoxicity (Wei et al., 2020). PAT not only endanger human health, but also affect food safety and nutrition by restricting access to healthy food. As a secondary metabolite produced by various molds, including *Byssochlamys, Penicillium,* and *Aspergillus*, patulin is particularly associated with *Penicillium expansum*, which is responsible for the rot of stored apples (Mukherjee et al., 2022). Apples are one of the most worldwide cultivated temperature fruits as its high nutritional value and seasonal availability (Feng et al., 2021). The maximum limit for PAT in apple juice set by the Codex Alimentarius Commission is 50 μg/L, which is same with the standard announced (50 μg/kg) by the food safety authorities from USA and China, while European Union decreased the maximum level to 10 μg/L of PAT in apple products (Cioates Negut et al., 2023). Generally, PAT is determined by chromatographic techniques, such as liquid chromatography-tandem mass spectrometry (LC/MS), gas chromatography-mass spectrometry (GC/MS) and HPLC. Although these methods are sensitive, reproducible, and accurate, they invariably require bulky, expensive instruments, skilled persons, laborious sample preparations (Datta et al., 2024). With the expanding global supply

* Correspondence to: School of Food and Biological Engineering, Jiangsu University, 301 Xuefu Road, Zhenjiang, Jiangsu 212013, China.
E-mail address: guozhiming@ujs.edu.cn (Z. Guo).

chains and increasing demand for food, there is a growing need for rapid, portable detection methods that are fast, cost-effective and require minimal sample treatment and handling.

In recent years, various nanosensors based on electrochemical and optical methods have been developed for onsite rapid detection of mycotoxins (Datta et al., 2024; Hermann et al., 2018; Xing et al., 2020). Among these detection methods, surface-enhanced Raman scattering (SERS) stands out as a versatile technique that offers high sensitivity and selectivity in food samples (Ma et al., 2024; Martinez and He, 2020; Xu et al., 2017). Being a vibrational spectroscopic technique, SERS provides structural information about the target analyte in complex media and has the potential for single molecule detection. Additionally, SERS signals have strong light stability, making SERS tags a promising substitute for conventional optical tags, such as quantum dots and fluorescent dyes, in various sensing applications. Consequently, labeled SERS techniques have been widely used in environmental monitoring, medical diagnosis, social security, and food safety (Wang et al., 2012; Wu et al., 2021). But SERS methods still faces challenges of high reproducibility, stability, high Raman enhancement signal and uniformity in quantitative analysis. The SERS signals are highly dependent on the morphology of the substrate (Yang et al., 2024). It is a big challenge to build up sensitive and stable SERS nanoprobes. SERS active core-molecule-shell nanoparticles provided strong and stable SERS signals, demonstrating admirable SERS performance in quantitative SERS analysis (Li et al., 2023; Lin et al., 2020). Ren et al. firstly reported this kind of plasmonic structure and subsequently employed the Raman molecule as an internal reference to mitigate external interferences, obtaining reliable quantitative analysis (Shen et al., 2015). Numerous similar SERS nanoprobes have been developed and utilized for highly sensitive analysis (Chen et al., 2022; Li et al., 2024). These CMS structures cannot prevent the internal molecules from external interference but also provide uniform and enhanced SERS hot spots. Nevertheless, this type of design is not capable of using the internal Raman molecules to detect external targets, as they are separated by the shell and cannot exhibit a target-activated SERS response. To detect the mycotoxin, it is generally necessary to additionally modify Raman molecules on the external surface (Jiao et al., 2022; Yin et al., 2024). However, this approach encounters the same issues as those faced by exposed Raman probes.

To realize sensitive and reliable SERS detection in mycotoxin detection, a possible approach is to implement an external switch, drawing inspiration from the fluorescence quenching strategy. Metal-organic frameworks (MOFs) are advanced porous materials with large surface areas, exhibiting great potential for the storage and transport of chemical cargoes (Samuel et al., 2024; Zhou et al., 2012). MOFs have demonstrated outstanding performance in variety of applications (Zhang et al., 2024). Additionally, their desirable traits such as great surface areas and customizable pore channels make them highly appealing for sensing applications in food safety (Wang et al., 2019). With the assistance of chemically programmable ligands, for example DNA, the manipulation of interparticle interactions was realized. In the hybrid nanoclusters, MOFs particle-satellite clusters hold promise for sensing applications (Wang et al., 2017).

The competitive binding strategy is a key approach for detecting small molecules (Li et al., 2020). This method relies on the competition between the recognition units and the small molecule for binding to a limited number of affinity ligands (Zhao et al., 2019; Guo et al., 2024). When a small molecule target is present, it displaces the affinity ligand from the recognition units, leading signal variation due to the unbound sensing probe. This strategy is commonly employed in the design of fluorescent sensor(Zhang et al., 2019). Given the stability and enhanced properties of SERS signals, it is significant to develop as a SERS sensor using this competitive binding strategy (Sun et al., 2021). The functional properties and tunable structure of MOFs have expanded the range of biosensing mechanisms when combined with other nanomaterials, leveraging the advantages of multi-materials systems (Ravipati and Badhulika, 2024). However, there is little report on SERS sensor based on MOFs for PAT detection.

In this study, we innovatively designed a SERS sensor based on CMS structure and MOFs, where the programmable ligand was utilized as a switch to regulate the SERS response, and the reliable signal-off SERS detection of PAT was obtained (Scheme 1). The MOFs-based particles were used as a substrate to anchor additional CMS nanostructures, forming nano-assemblies with the assistance of programmable ligands. This approach significantly amplified the SERS signals. Through competitive binding, the signal was quenched in the presence of PAT, which enhanced the signal variation at lower concentration of PAT without interference with the SERS spectra. The MOFs, (Uio-66) was synthesized with functionalization of complementary probe, while the plasmonic CMS structure embedded in SERS tags was modified by capture probe for PAT. The relevance of the SERS performance to the MOFs structure and the shell thickness was explored systematically, it was found that the MOFs substrate further magnified the SERS signals by gathering more CMS structure in one particle, and the silver shell could block the internal signal by inhibiting the penetration of excitation laser and emission SERS signals. Under optimize conditions, these two nanocomposites were assembled through DNA hybridization with high SERS signals. In the presence of PAT, the PAT bound to the capture aptamer and decomposed the assembly, leading to the shedding of the plasmonic nanoparticles into the supernatant. Here, the signal changes were manipulated by the target-responsive duplex DNA sequence, avoiding the directing interaction between the target and Raman molecule. Benefiting from the CMS plasmonic structure and switchable SERS mechanism, the SERS sensor showed a high sensitivity, good selectivity, and rapid response for PAT detection in apple juice. This strategy provides a new solution for monitoring chemical contaminations in environmental, medical, and food safety field.

2. Materials and methods

2.1. Materials

Zirconium(IV) chloride (98 %), 2-Aminoterephthalic acid (>98 %),4-mercaptobenzoic acid (4MBA), and Tris(2-carboxyethyl) phosphine (TCEP) were purchased from Aladdin Scientific Corp. (China). Acetic acid (>99.8 %), N,N-Dimethylformamide (>99.5 %), Sodium borohydride (>98 %) and Hydroxylammonium chloride (99 %) were obtained by China National Pharmaceutical Group Co Ltd (Sinopharm). The complementary probe (cDNA) and capture probe (aptamer) were prepared by GenScript Biotech Corporation. Ultrapure water was prepared in our lab using a laboratory water purification system (18.2 MΩ·cm).

2.2. Instruments and characterizations

D8-advance instrument (Bruker AXS Ltd., Germany) was used to acquire the nanoparticles' X-ray diffraction (XRD) pattern. The nanoparticles' Fourier transform infrared spectra (FTIR) transmittance spectra were recorded by a FTIR spectrometer (WQF-510A FT-IR, Beijing Rayleigh Analytical Instrument Co., Ltd., China) in the range 4000–650 cm^{-1} at room temperature. The SEM images were obtained by field emission scanning electron microscopy (SEM, JEOL Ltd., Japan). SPLD-RAMAN-785-Q Spectrometer (Hangzhou SPL photonics Co Ltd., China) with a laser excitation wavelength of 785 nm was used to record all the SERS measurements.

2.3. Synthesis of UiO-66@Au

Hydrothermal synthesis method was employed to prepare zirconium-based MOFs material (Cao et al., 2023). UiO-66: zirconium tetrachloride ($ZrCl_4$ 62.9 mg) and 2-amino terephthalic acid ($H_2BDC\text{-}NH_2$ 48.9 mg) was placed in a 250 mL beaker, and 7.2 mL of

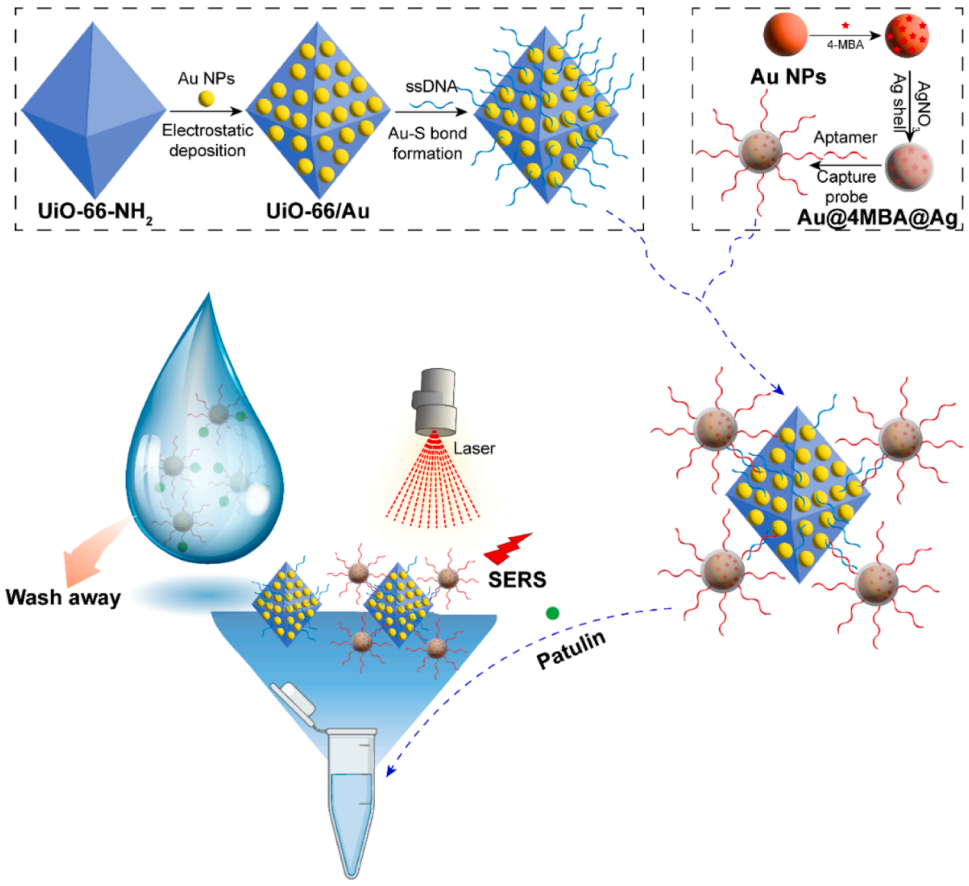

Scheme 1. Schematic illustration for the synthesis and sensing mechanism of the developed sensor for detecting PAT in apple juice.

acetic acid (Hac) and 60 mL of N,N′-dimethylformamide (DMF) were added to it. The mixture was sonicated for 30 min until completely dissolved. After dissolution, it was transferred to a high-pressure reaction vessel equipped with a polytetrafluoroethylene liner, heated to 120°C for 24 h. Then the reaction vessel was cooled to room temperature, yielding a yellowish solution. The generated solution was centrifuged at 9000 rpm for 5 min, and the resulting UiO-66 precipitate was collected. The precipitate was washed alternately by DMF and anhydrous ethanol for 5–6 times, then dried in a vacuum oven at 60°C for 12 h to obtain UiO-66(NH_2) as a milky white solid powder.

Decoration of MOFs with gold nanoparticles (Zhang et al., 2021): 1.8 mg of UiO-66 was dispersed in 2 mL of water, followed by addition of 20 mL of chloroauric acid solution (0.25 mM), and vigorously stirred at 4°C for 5 min. Then, 0.1 mL of sodium citrate solution (5 % wt) and 1 mL of freshly prepared sodium borohydride solution (0.01 M) were rapidly added sequentially. The solution immediately changed from light yellow to reddish-brown. After continuing stirring for 6 min, the reaction was stopped by centrifugation at 9000 rpm for 10 min, the supernatant was discarded, and the precipitate was dispersed in 8 mL of water, denoted as UiO-66@Au seed.

0.8 mL of above seed solution was added to 7.2 mL of $HAuCl_4$ (0.27 mM) solution under stirring at 800 rpm, sodium citrate solution was added to achieve a molar ratio of 3:1 with $HAuCl_4$, then 76 μL of hydroxylamine hydrochloride solution (40 mM) was added. The reaction was stirred at room temperature for 30 min, yielding UiO-66@Au.

2.4. Preparation of UiO-66@Au modified by complementary probe

The complementary DNA (cDNA: SH-5'-GCGGGTTGGCGGGCC-3') (10 μM) and 10 mM of TCEP was mixed with the same volume, and the mixture was incubated at 37°C for 30 minutes to activate the thiol groups. Then, 60 μL of the activated cDNA solution was added to 440 μL of UiO-66@Au solution, which were incubated at 37°C for 12 h. Afterward, the nanocomposite was purified by centrifugation and resuspend in 500 μL of buffer solution, obtaining the UiO-66@Au-cDNA.

2.5. Preparation of Au@4MBA@Ag

Gold nanoparticles were prepared as the core firstly. 100 mL of $HAuCl_4$ solution (0.01 %) was heated to boiling. Then 1.6 mL of sodium citrate solution (1 %) was added quickly, followed by gentle stirring for 6 min. The color of the solution changes from light yellow to deep purple and then gradually to wine red. The reaction was stopped in an ice bath, and the solution was stored at 4°C for later use.

5 mL of the Au solution was mixed with the Raman molecule (4MBA) (5×10^{-6} M), and stirred at 400 rpm for 1 h to promote Au-S bond formation. The unbound molecules were removed by centrifugation at 9000 rpm for 9 min. Then, 100 μL of sodium citrate (1 %) and 250 μL of ascorbic acid (1 mM) were added to the centrifuge tube, under stirring at 800 rpm, followed by slow addition of 300 μL of 10 mM $AgNO_3$ (approximately 15 s/drop). The reaction was stirred for 30 min, continually, then centrifugation (8500 rpm, 15 min) was conducted to remove the supernatant. The final nanoparticles (Au@4MBA@Ag) were resuspended in 1 mL of water.

2.6. Preparation of Au@4MBA@Ag functionalized by capture probe

30 μL of capture probe (aptamer: 5'-GGCC CGCC AACC CGCA TCAT CTAC ACTG ATAT TTTA CCTT-3'-SH) (10 μM) was mixed with 30 μL of TCEP (10 mM), and incubated at 37°C for 30 min to activate the thiol groups. Then, the mixture was added to 440 μL of Au@4MBA@Ag solution, with incubation at 37°C for 12 h. Afterward, the nano-

hybridizations were purified by centrifugation and resuspend in 500 μL of buffer solution to obtain the final Au@4MBA@Ag-apt.

2.7. Preparation of the nanocomposite for PAT assay

The UiO-66@Au-cDNA was mixed with Au@4MBA@Ag-apt, and incubated at 37°C for 2 h. Then the unbound Au@4MBA@Ag-apt was removed by centrifugation at 4500 rpm for 5 min, and precipitate nanocomposite was redispersed in buffer solution.

Various PAT standard solutions (100 μL, 0.001, 0.01, 0.05, 0.1, 0.5, 1, 10, 50, 100, 250, and 1000 ng/mL) were mixed with 100 μL of nano-hybridization respectively. The mixture was incubated for 1.5 h, then the dissociated Au@4MBA@Ag-apt was removed by centrifugation at 4500 rpm. The reminded nano-hybridizations were redispersed 100 μL of buffer solution. Then 2 μL of solution was dropped on a aluminum foil for SERS measurement. The testing parameters are: laser 638 nm, power 100 mW, accumulation time 5 s. Each concentration was tested for 5 times to get the averaged spectra. The linear relationship was built based on the intensity of characteristic peaks of 4MBA (at 1586 cm^{-1}) *vs* the concentration of PAT.

2.8. Application of detecting spiked samples

Apple and commercial apple juice were selected as real samples to verify the practical feasibility of our sensor. 5 g of fruit pulp was mixed with PAT standard solution to make different spiked samples (20, 50, 100 μg/kg). Then, 10 mL of water and 20 mg of pectinase were added to the fruit pulp and incubated at 40°C water bath for 1 h for enzymatic hydrolysis. Next, 15 mL of extraction solution (acetonitrile: water = 9:1) was added to different spiked sample tubes. The mixture was shaken for 15 min, then centrifuged at 6500 rpm for 15 min, the precipitate was discarded, and the volume was adjusted to 25 mL. Additionally, 5 mL of commercial apple juice was mixed with PAT standard solution, to get the spiked samples (25, 75, 125 μg/kg, respectively), then 20 mL of ultra-pure water was added to obtain the PAT extraction solution from the juice.

The amount of PAT in spiked samples was detected by our SERS sensor, and calculated based on the following equation:

$$X = \frac{\rho \times V}{m}$$

where X represents the PAT content in the spiked samples (μg/kg), ρ represents the PAT concentration in the sample solution calculated according to the standard curve (ng/mL), V represents the final volume of the sample after pretreatment (mL), and m represents the sample mass (g).

The Recovery rate (= Detection value/Spiked value × 100 %) was used to verify the accuracy of the developed method.

3. Results and Discussion

3.1. Characterizations of UiO-66 and UiO-66@Au

The UiO-66 nanoparticles were synthesized based on a hydrothermal method (Hu et al., 2015). As the scanning electron microscopy (SEM) image showed, the UiO-66 exhibited an octahedral crystal structure (Fig. 1a). The FTIR spectroscopy was carried out to study the chemical

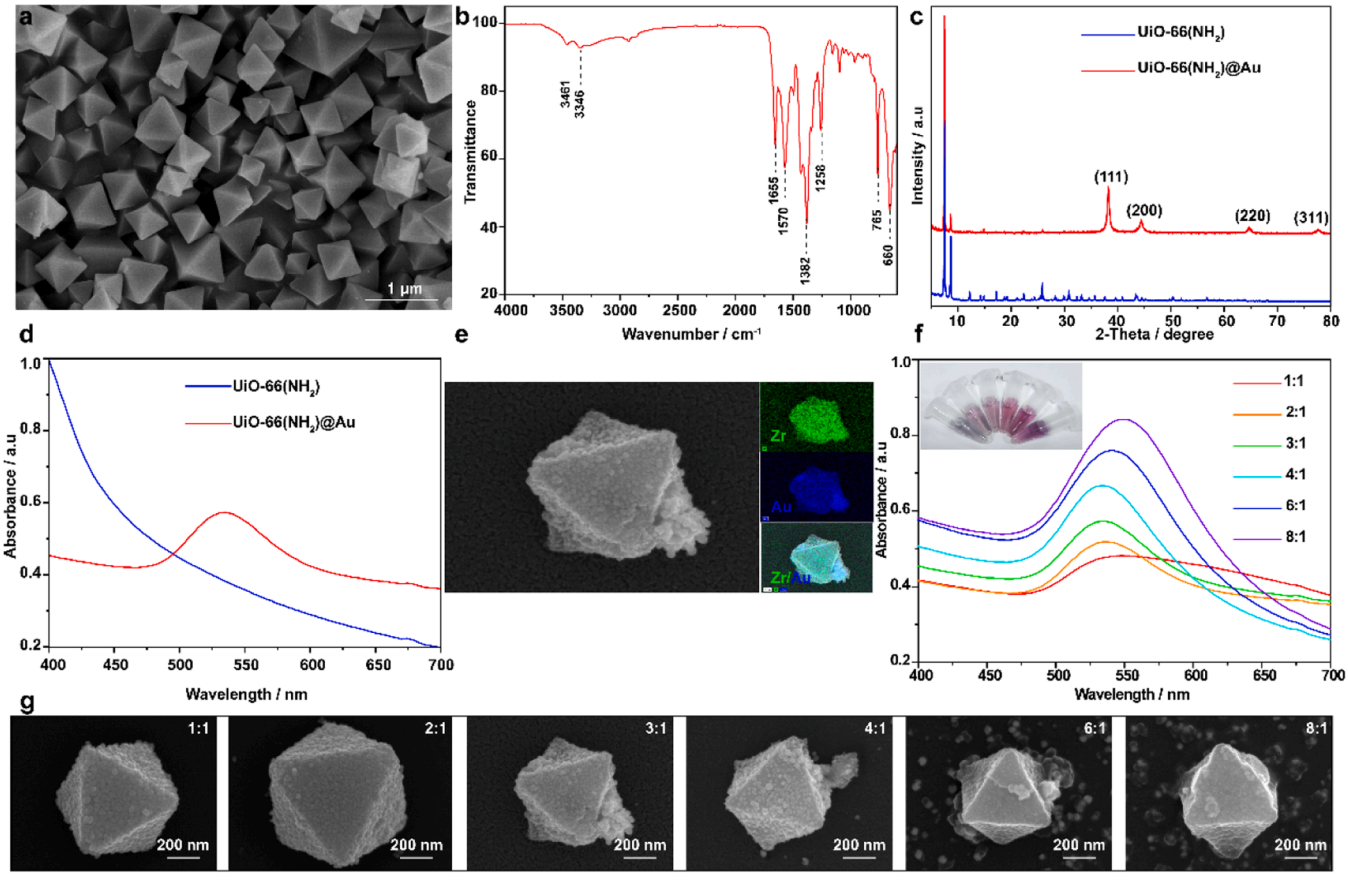

Fig. 1. (a) SEM image of UiO-66. (b) The FTIR spectra of UiO-66. (c) PXRD patterns of UiO-66 and UiO-66@Au. (d) UV–vis spectra of UiO-66 and UiO-66@Au. (e) SEM image of UiO-66@Au and the corresponding EDS elemental mapping images showing Zr (green) and Au (blue) in the same area. (f) The UV–vis spectra of UiO-66@Au, which were prepared under various molar ratio of $Na_3Cit/HAuCl_4$. (g) The SEM images of UiO-66@Au, which were prepared under various molar ratio of $Na_3Cit/HAuCl_4$.

structure of the MOFs (Fig. 1b). The peaks at 660 cm ^{1} and 765 cm ^{1}, respectively, originated from the longitudinal and transverse vibrations of Zr-O bonds. The four peaks appeared at 3461 cm ^{1}, 3346 cm ^{1}, 1655 cm ^{1}, 1382 cm ^{1}, and 1258 cm ^{1} belonged to the absorption peaks of ν_{as} (N-H), ν_{s} (N-H), δ(N-H), ν(C-H) and ν(C-H) in 2-aminoterephthalic acid (Olorunyomi et al., 2022). The peak at 1570 cm ^{1} was assigned to C-O-Zr (Liu et al., 2019). The powder X-ray diffraction (PXRD) pattern revealed the crystallinity of UiO-66 (2θ=7.53° and 2θ=8.65°) (Fig. 1c), which was analogous to a previous report (Xiang et al., 2020). The UiO-66 exhibited a preferable adsorption capacity to $AuCl_4^-$, as the smaller size of $AuCl_4^-$ (~5.4 Å) than the pore size of UiO-66 (6 Å) (Lin et al., 2017; Lin et al., 2019). Later, the $AuCl_4^-$ was reduced by sodium citrate and sodium borohydride, Au nanoparticles were in situ prepared on the surface of MOFs, leading to the successful construction of UiO-66@Au. From the PXRD pattern, four new diffraction peaks emerged at 38.25°, 44.35°, 64.66°, and 77.65° appeared, in agreement with the pattern of gold nanoparticles corresponding the (111), (200), (220) and (311) panels (Radziuk et al., 2010). From the UV–vis absorption spectra (Fig. 1d), the UiO-66 had no absorption in the test range, while UiO-66@Au showed a new absorption peak at 535 nm which is similar with that of gold nanoparticles. The amplified SEM image (Fig. 1e) of UiO-66@Au showed the particle was rough with small particles on the surface. But the octahedral structure of UiO-66 was unchanged after the deposition of Au nanoparticles, confirmed the structural stability of UiO-66. The Au NPs was further proved by the related energy-dispersive X-ray spectroscopy (EDS) elemental mapping analysis, the elemental mapping images indicated the homogeneous distribution of Zr (green color) and Au (blue color) on the entire framework (Fig. 1e) and the successful synthesis of UiO-66@Au. The corresponding elemental analysis spectra was shown in Fig. S1, indicating the presence of Au and Zr element.

To make sure more cDNA could be conjugated to the surface of UiO-66@Au, it was necessary to have more gold nanoparticles on the surface, but it also needed to keep the balance between the amount of gold nanoparticles and the morphology of final particles. The deposition of Au nanoparticles was tuned by the molar ratio of $Na_3Cit/HAuCl_4$, from 1:1–8:1. The corresponding UV–vis absorption spectra and samples' color of UiO-66@Au were shown in Fig. 1f. These data demonstrated the formation of gold nanoparticles, with the color changed from bule to purplish red. From 1:1–3:1, these nanoparticles exhibit an intense peak absorption peak around 536 nm with a blue-shift, which might be associated with the diploe coupling in the Au nanoparticles (Jenkins et al., 2014). Nevertheless, the spectra are red shit after 4:1 and the absorption peaks become higher and broader. This may be induced by the formation of independent gold nanoparticles and the aggregation of particles. We observed that a 3:1 ratio is necessary to coat uniformly MOFs (Fig. 1g). The SEM images of 3:1 UiO-66@Au showed that it has rougher and denser surface than that under the lower ratio (1:1 and 2:1), and the relatively stable structure. The close distance between gold nanoparticles might accelerate the particles' diploe coupling, which was consistent with the phenomenon of blue-shift in the UV–vis spectra. We have increased the molar ratio to examine the role of excess gold. We found that under these conditions the size of gold particles became bigger (4:1). Further successive enlargement of the ratio (6:1, 8:1) resulted in a dissociation of gold nanoparticles. This meant that during these reactions the two types of gold nanoparticles were formed and led to nonuniform coating (Fig. 1g). This was possibly cause by the faster reaction kineties under higher ratio, the gold nanoparticles were formed directly by the reduction of $HAuCl_4$ with Na_3Cit in the aqueous solution. We also tested the stability of UiO-66@Au by storage at 4 °C for 180 days. The stability was evaluated by the fluctuation of the ability of SERS enhancement at specified time interval (Fig. S2). After a certain storage period, UiO-66@Au was mixed with 4MBA (10 ^{4} M) for 30 min, followed by Raman test. After 7 times measurement, the RSD of the intensity of characteristic peak was only 2.68 %, and during each measurement the RSD of this was below 5 %. These results showed the gold nanoparticles on UiO-66@Au did not experience any decomposition, demonstrating the good stability of UiO-66@Au.

3.2. Preparation of Au@4MBA@Ag

The plasmonic nanostructure of Au@4MBA@Ag was synthesized step by step (Xue et al., 2024). First, the gold nanoparticles were synthesized by the citrate-based reduction method (Ji et al., 2007). The UV–vis spectra showed the characteristic adsorption peak of Au nanoparticles at 512 nm (Fig. 2a). Later, the Raman molecule (4MBA) was conjugated to the surface of Au nanoparticles through the formation of Au-S bond. Finally, The Ag coating on the surface of Au nanoparticles was achieved by reducing $AgNO_3$ with a strong reducing agent (a mixture of sodium citrate and ascorbic acid) as their similar lattice constant (Au (0.408) and Ag (0.409) with a difference of 0.2 %) (Ma et al., 2010). The finalized bimetallic core-shell nanoparticles (Au@4MBA@Ag) displayed two characteristic peaks located at 407 nm and 486 nm, corresponding to the Ag shell and Au core, respectively (Fig. 2a), while the blue-shifted surface plasmon absorbance of Au indicated coupling between the Ag layers and Au (Haidar et al., 2019). The core-shell structure was further verified in detail by TEM. In the TEM images, the core-shell structure showed a clear boundary with the central dark and outer bright layer contrast, representative of the Au (core) and Ag (shell) (Fig. 2b).

To optimize the SERS signals, various amount of 4MBA and $AgNO_3$ were used in the preparation of Au@4MBA@Ag. The Au nanoparticles were incubated with different concentration of 4MBA, with increased concentrations, the Raman signals intensity of 4MBA also increased (Fig. 2c). At the concentration of 5×10^{6} mol/L, the Raman intensity got the maximum, indicating the balance between the Raman enhancement and the dispersity of nanoparticles. We found, at a higher concentration, 4MBA induced the aggregation of Au nanoparticles, and the slight Raman intensity decrease. The plasmonic Ag shell can interfere with the SERS performance of the embedded Raman molecule (Dai et al., 2020). To achieve the maximum SERS enhancement, Ag shell of varying thickness were synthesized by adjusting the amount of $AgNO_3$ during the preparation process. As the volume of $AgNO_3$ increased from 150 μL to 400 μL, the thickness of the Ag shell also increased. This was confirmed by the UV–vis spectra, which showed a shift of the plasmon band associated with Ag shell from 400 nm to 410 nm, accompanied by an increase in intensity. Meanwhile, the characteristic peak of the Au core at around 486 nm gradually dispersed (Fig. 2d). This resulted in increased Raman intensity up to an $AgNO_3$ volume of 300 μL. However, beyond this optimum amount, the thicker Ag shell began to block the emission of SERS signals, conversely, resulting in a decrease in Raman intensity (Fig. 2e). These findings underscore the importance of optimizing the Ag shell thickness for achieving the best SERS performance. In addition, the SERS enhanced performance of different substrates was investigated under the same conditions (the same testing parameters and the same concentrations of 4MBA) (Fig. 2f). The intense Raman scattering peaks of the aromatic ring vibrations (ν_{8a}) at 1582 cm ^{1} in 4MBA in the spectra of Au@4MBA@Ag was 10 times higher than that of Au@4MBA, demonstrating the core-molecule-shell structure could provide significantly enhanced Raman scattering and enhanced the sensitivity of PAT detection effectively.

3.3. Conjugation of aptamers and assembly of SERS sensor

The complementary probe and capture probe were conjugated to the surface of UiO-66@Au and Au@4MBA@Ag, respectively, through the formation of strong Au-S bonds and Ag-S bonds. The successful conjugation was confirmed by UV–vis spectra and zeta potential measurements. A new band was observed at 260 nm, corresponding to the characteristic peak of aptamer, derived from the nucleic acid bases (Fig. 3a and Fig. 3b). Because of the presence citrate ions on the gold surface, the zeta potential values of UiO-66@Au and Au@4MBA@Ag

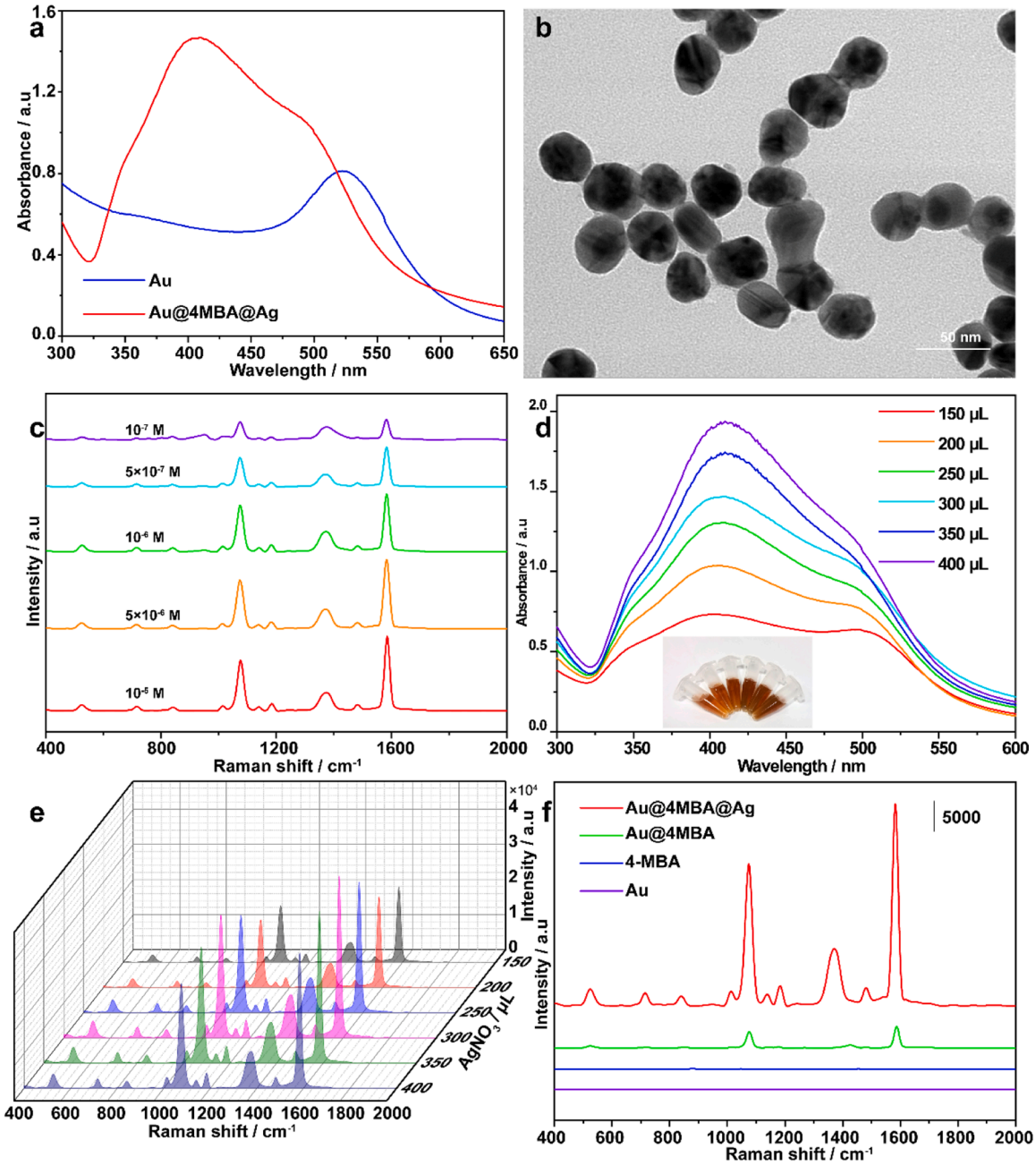

Fig. 2. (a) The UV–vis spectra of Au nanoparticles and Au@4MBA@Ag nanoparticles. (b) TEM image of Au@4MBA@Ag. (c) The SERS spectra of Au nanoparticles by incubating with various concentrations of 4-MBA. (d) The UV–vis spectra of Au@4MBA@Ag, which was prepared by using different amount of $AgNO_3$ in the preparation process. Insert, the images of aqueous Au@4MBA@Ag solution by increasing the amount of $AgNO_3$ (from left to right). (e) The SERS spectra of Au@4MBA@Ag, which was prepared by using different amount of $AgNO_3$ in the preparation process. (f) Raman spectra of Au, 4MBA, Au@4MBA, and Au@4MBA@Ag, the Raman spectra intensity of 4MBA were compared at the same concentration.

were 38.01 mV and 33.21 mV, respectively, but they became more negatively charged after the modification (-44.3 mv, and 37.69 mv) (Fig. 3a and Fig. 3b, insert). This increase in negative charge is attributed to the negatively charged nucleic acids (Röthlisberger and Hollenstein, 2018), indicating successful aptamer conjugation. The maximum functionalization of capture probe on the surface of Au@4MBA@Ag was also explored by increasing the concentration of capture probe in the reaction of conjugating aptamer. The amount of capture probe on Au@4MBA@Ag-apt was monitored by UV–vis spectroscopy measurement (Fig. S3). When the concentration was above 600 nM, the characteristic adsorption peak of aptamer became stable, indicating the saturation of aptamer on the surface.

The SERS sensor was prepared through the hybridization of complementary probes with the capture probe in UiO-66@Au-cDNA and Au@4MBA@Ag-apt, respectively. The SERS signals of the assemblies increased as the mass ratio of UiO-66@Au-cDNA to Au@4MBA@Ag-apt was increased (Fig. 3c). When the ratio was 1:4, the SERS intensity got the maximum which was chosen for forming the assemblies. As the large size of UiO-66 (~200 nm), the SERS sensor could be easily separated by centrifugation. With the same amount of Au@4MBA@Ag, the SERS sensor could be easily separated under low speed of centrifugation (4500 rpm, 5 min), while only a small part of Au@4MBA@Ag was separated under the same condition (Fig. 3d). These results demonstrate the feasibility of the SERS sensor for sensing application based on

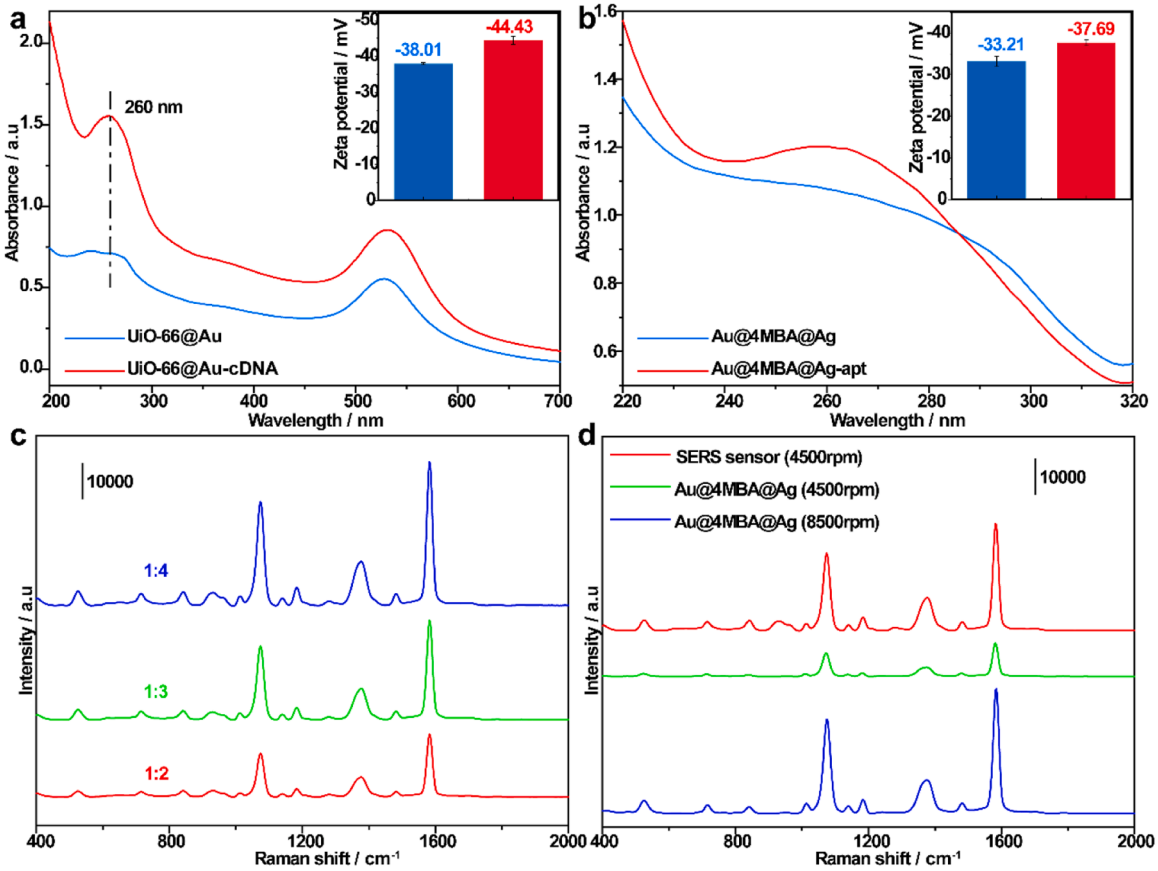

Fig. 3. (a) The UV–vis spectra of UiO-66@Au before and after the modification of aptamer. Inset, the corresponding zeta potential of UiO-66@Au and UiO-66@Au-cDNA. (b) The UV–vis spectra of Au@4MBA@Ag before and after the modification of aptamer. Inset, the corresponding zeta potential of Au@4MBA@Ag and u@4MBA@Ag-apt. (c) The Raman spectra of the developed SERS sensor, which was assembled from various mass ratio of UiO-66@Au-cDNA to Au@4MBA@Ag-apt (from 1:2–1:4). (d) The Raman spectra of different types of nanoparticles with same amount of Au@4MBA@Ag, which were redispersed in same volume after centrifugation.

competitive binding.

3.4. Analytical application and selectivity evaluation

The Raman reporters embedded in Au@4MBA@Ag-apt produce quantitative SERS signals, avoiding the interference from samples and the state of nanoparticles. Therefore, the fabricated SERS sensor displayed the potential application for the detection of PAT. The Raman peak at 1582 cm ^{1} showed the maximum intensity and was chosen as the discrimination position for the quantitative analysis of PAT. In the presence of PAT, the higher selectivity of capture probes for the targets induced structural variations in the aptamers and the dissociation of Au@4MBA@Ag-apt from MOFs. The remaining Au@4MBA@Ag-apt and UiO-66@Au-cDNA assemblies were completely separated by centrifugation, and there are only dissociated Au@4MBA@Ag-apt in supernatant. SERS intensities at 1582 cm ^{1} decreased with increasing concentrations PAT of PAT from 0.01 ng/mL to 1000 ng/mL (Fig. 4a). The discrimination of PAT was saturated at higher concentration. The repeatability and signal stability was evaluated by testing 49 points in one sample, and the RSD was only 6.33 % (Fig. S4). This was due to the superiority of CMS structure, demonstrating the good performance of this SERS sensor in sensing applications. A standard curve between SERS intensity at 1582 cm ^{1} and PAT concentration (0.05–250 ng/mL) was established with a good linear relationship (Fig. 4b). The limit of detection (LOD) is calculated to be 0.02 ng/mL based on 3σ criterion. A summary of previous works on PAT detection is presented in table S1, confirming that the developed SERS sensor enables quantitative detection of PAT with a low LOD. The selectivity of the sensor was explored using Alternariol (AOH) and Ochratoxin A (OTA). At the same concentration of PAT, the sensor exhibited an equivalent response when detecting PAT in the presence of either AOH or OTA. Notably, there was no significant decline in the sensor's response when AOH and OTA were detected separately at the same concentrations (Fig. 4c). These findings demonstrated that the SERS sensor could effectively distinguish PAT from other mycotoxins by displaying a highly selective decrease in the SERS response.

To evaluate the sensor's performance in a complex matrix, spiked apple juice samples were analyzed using the developed competitive SERS sensor. Various concentrations of PAT in spiked samples, including both fresh apples and commercial apple juice, were initially detected using standard HPLC method (Table 1), with recovery rates ranging from 90.22 % to 94.64 %. The results obtained from our SERS sensor (Fig. 4d) showed a strong correlation with those from HPLC analysis, with recovery rates ranging from 91.98 ± 4.47 % to 102.94 ± 4.97 %. These results suggested that our competitive SERS sensor has considerable potential for reliably detecting PAT in apples.

4. Conclusions

In this study, we developed a novel switchable SERS sensor based on competitive binding for ultrarace detection of PAT. The programmable ligand, namely the duplex DNA sequence (aptamer + cDNA) serving as a switch was utilized to connect CMS structure and MOFs, and enabled the SERS sensor to carry out signal-off sensing without interfering the internal Raman molecule. The UiO-66 further increased the SERS intensity of one particle, making it possible for highly sensitive detection. The

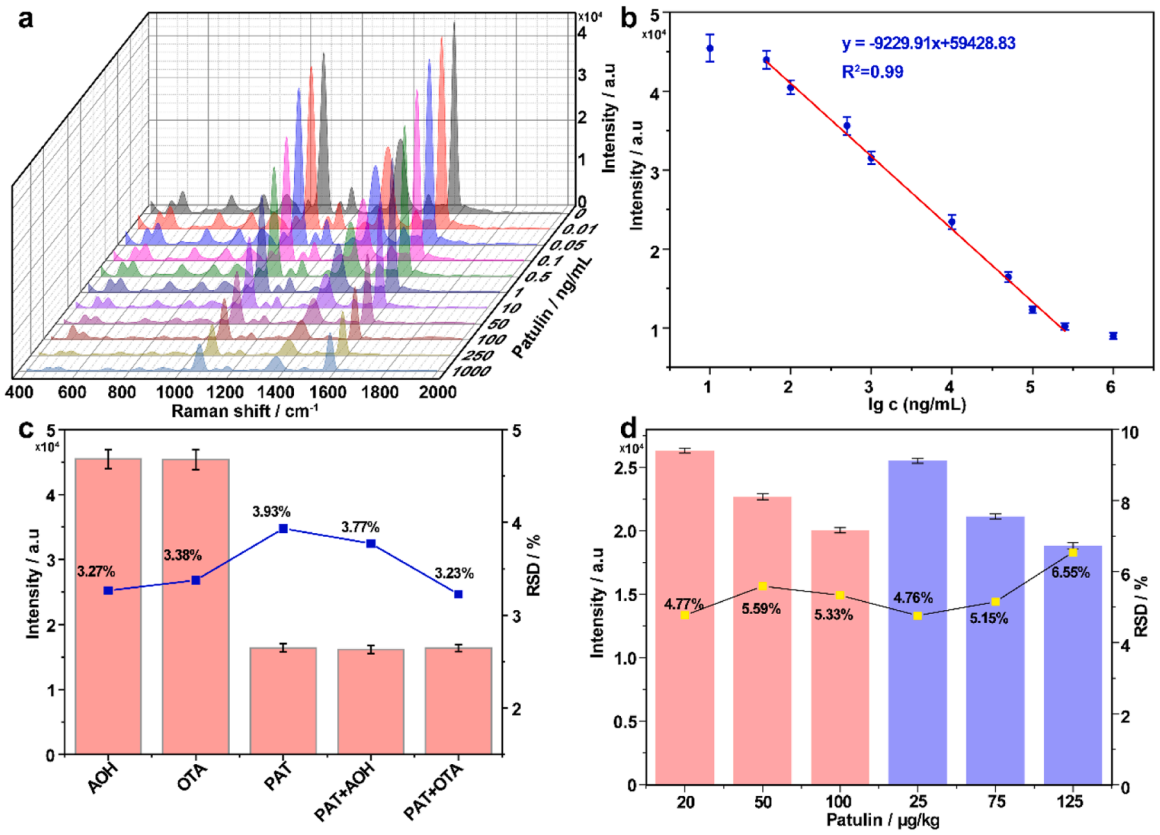

Fig. 4. (a) SERS spectra obtained by adding different concentrations of PAT to the SERS sensor. (b) The intensity correlation curve between PAT concentration and Raman characteristic peak at 1582 cm^{-1}. (c) The selectivity test of the developed SERS sensor against other mycotoxins (AOH: Alternariol, OTA: Ochratoxin A). (d) The applications of the developed sensor in spiked samples with various concentrations of PAT (red bars: apples, blue bars: commercial apple juice).

Table 1
Recovery rate of PAT spiked in apples and apple juice samples detected by the develop SERS sensor and HPLC analysis.

Spiked samples	PAT (μg/kg)	SERS			HPLC	
		Detected concentration (μg/kg)	Mean recovery (%)	RSD (%)	Detected concentration (μg/kg)	Mean recovery (%)
Apples	20.00	18.40	91.98	4.47	18.93	94.64
	50.00	51.47	102.94	4.97	46.03	92.05
	100.00	96.10	96.10	4.25	90.22	90.22
Apple juice	25.00	24.31	97.22	4.49	23.65	94.61
	75.00	70.82	94.43	4.12	70.58	94.11
	125.00	126.27	101.02	3.77	112.88	90.31

*RSD, relative standard deviation

CMS plasmonic nanostructure provided enhanced and uniform hot spots, but the Ag shell could also hinder the SERS signal at greater depths. We investigated the optimized conditions for making the Au@4MBA@Ag-apt and UiO-66@Au-cDNA assemblies. The proposed sensor showed a wide detection range, low detection limit, and high selectivity, with great potential for real-world applications in apples and apple juice. This SERS approach is anticipated to have extensive applications in food safety, environmental protection, diagnosis and biosensing.

In future research, several considerations should also be taken into account. Although "signal-off" sensing offers advantages such as a broad linear detection scope and simple fabrication, this strategy is constrained by the maximal level of signal reduction. Specifically, the obtained signal can never get zero (i.e., 100 % signal reduction), while the "signal-on" sensing can achieve substantial signal gain due to a much lower background approaching zero in the absence of a target, along with a sufficient signal-to-background ratio. Furthermore, false positive results may arise following the degradation of the duplex DNA structure, which could impact the reliability of the sensor. To enhance the performance of the developed sensor, future research should focus on improving the sensitivity of the signal and enhancing the sensor's anti-interference capabilities. This may involve exploring alternative sensing strategies, optimizing the binding mechanisms, and developing more robust recognition elements to minimize the effects of potential interferents. Such advancements will pave the way for more reliable and effective applications in food safety and environmental monitoring.

Author statement

We, the undersigned, declare that this manuscript is original, has not been published before and is not currently being considered for publication elsewhere. We confirm that the manuscript has been read and approved by all named authors and that there are no other persons who satisfied the criteria for authorship but are not listed. We further confirm that the order of authors listed in the manuscript has been approved by all of us. We understand that the Corresponding Author is the sole

contact for the Editorial process. He is responsible for communicating with the other authors about progress, submissions of revisions and final approval of proofs.

CRediT authorship contribution statement

Yang Zhang: Writing – original draft, Investigation, Funding acquisition, Formal analysis, Data curation. **Limei Yin:** Data curation. **Xinchen Wu:** Formal analysis, Data curation. **Chuping Zhao:** Data curation. **Ruiyun Zhou:** Data curation. **Tianxi Yang:** Writing – review & editing. **Pierre Picchetti:** Writing – review & editing. **Zhiming Guo:** Supervision, Funding acquisition. **Xiaobo Zou:** Supervision. **Zhepeng Zhang:** Data curation. **Shanshan Xue:** Data curation.

Declaration of Competing Interest

The authors declare that they have no known competing financial interests or personal relationships that could have appeared to influence the work reported in this paper.

Acknowledgements

This research was funded by the National Natural Science Foundation of China (W2412103), Key R&D Project of Jiangsu Province (BE2022363), Natural Science Foundation of Jiangsu Province (BK20210748) and Advanced Talents Science Foundation of Jiangsu University (No. 21JDG055).

Data availability

Data will be made available on request.

References

Cao, J., Xu, Z., Chen, Y., Li, S., Jiang, Y., Bai, L., Yu, H., Li, H., Bian, Z., 2023. Tailoring the asymmetric structure of NH_2-UiO-66 metal-organic frameworks for light-promoted selective and efficient gold extraction and separation (Artticle). Angew. Chem. Int. Ed. 62, e202302202. https://doi.org/10.1002/anie.202302202.

Chen, S., Fan, J., Lv, M., Hua, C., Liang, G., Zhang, S., 2022. Internal standard assisted surface-enhanced raman scattering nanoprobe with 4-NTP as recognition unit for ratiometric imaging hydrogen sulfide in living cells. Anal. Chem. 94, 14675–14681. https://doi.org/10.1021/acs.analchem.2c02961.

Cioates Negut, C., Stefan-van Staden, R.-I., van Staden, J.F., 2023. Fast screening test of apple juice and surface water for patulin recognition and quantification. ACS Food Sci. Technol. 3, 1248–1254. https://doi.org/10.1021/acsfoodscitech.3c00136.

Dai, X., Song, Z.L., Song, W., Zhang, J., Fan, G.C., Wang, W., Luo, X., 2020. Shell-switchable SERS blocking strategy for reliable signal-on sers sensing in living cells: detecting an external target without affecting the internal raman molecule. Anal. Chem. 92, 11469–11475. https://doi.org/10.1021/acs.analchem.0c02747.

Datta, B., Bhatt, P., Dutta, G., 2024. A Redox mediator-free highly selective and sensitive electrochemical aptasensor for patulin mycotoxin detection in apple juice using Ni–NiO pseudocapacitive nanomaterials. J. Agric. Food Chem. 72, 5993–6005. https://doi.org/10.1021/acs.jafc.3c07886.

Feng, S., Yi, J., Li, X., Wu, X., Zhao, Y., Ma, Y., Bi, J., 2021. Systematic review of phenolic compounds in apple fruits: compositions, distribution, absorption, metabolism, and processing stability. J. Agric. Food Chem. 69, 7–27. https://doi.org/10.1021/acs.jafc.0c05481.

Guo, Z., Zheng, Y., Yin, L., Xue, S., Ma, L., Zhou, R., Zou, X., 2024. Flexible Au@ AgNRs/MAA/PDMS-based SERS sensor coupled with intelligent algorithms for in-situ detection of thiram on apple. Sensors and Actuators B: Chemical 404, 135303. https://doi.org/10.1016/j.snb.2024.135303.

Haidar, I., Day, A., Decorse, P., Lau-Truong, S., Chevillot-Biraud, A., Aubard, J., Félidj, N., Boubekeur-Lecaque, L., 2019. Tailoring the shape of anisotropic core–shell au–ag nanoparticles in dimethyl sulfoxide. Chem. Mater. 31, 2741–2749. https://doi.org/10.1021/acs.chemmater.8b04735.

Haque, M.A., Wang, Y., Shen, Z., Li, X., Saleemi, M.K., He, C., 2020. Mycotoxin contamination and control strategy in human, domestic animal and poultry: a review. Article e104095 Microb. Pathog. 142. https://doi.org/10.1016/j.micpath.2020.104095.

Hermann, C.A., Duerkop, A., Baeumner, A.J., 2018. Food safety analysis enabled through biological and synthetic materials: a critical review of current trends. Anal. Chem. 91, 569–587. https://doi.org/10.1021/acs.analchem.8b04598.

Hu, Z., Peng, Y., Kang, Z., Qian, Y., Zhao, D., 2015. A modulated hydrothermal (MHT) approach for the facile synthesis of UiO-66-type MOFs. Inorg. Chem. 54, 4862–4868. https://doi.org/10.1021/acs.inorgchem.5b00435.

Jenkins, J.A., Zhou, Y., Thota, S., Tian, X., Zhao, X., Zou, S., Zhao, J., 2014. Blue-shifted narrow localized surface plasmon resonance from dipole coupling in gold nanoparticle random arrays. J. Phys. Chem. C. 118, 26276–26283. https://doi.org/10.1021/jp508181g.

Ji, X., Song, X., Li, J., Bai, Y., Yang, W., Peng, X., 2007. Size control of gold nanocrystals in citrate reduction: the third role of citrate. J. Am. Chem. Soc. 129, 13939–13948. https://doi.org/10.1021/ja074447k.

Jiao, S., Liu, J., Sun, J., Chang, Y., Wang, S., Dai, S., Xu, R., Dou, M., Li, Q., Wang, J., Li, J., 2022. A highly sensitive and reproducible multiplex mycotoxin SERS array based on AuNPs-loaded inverse opal silica photonic crystal microsphere. Article 3131245 Sens Actuators B Chem. 355. https://doi.org/10.1016/j.snb.2021.131245.

Kabak, B., Dobson, A.D.W., Var, I., 2006. Strategies to prevent mycotoxin contamination of food and animal feed: a review. Crit. Rev. Food Sci. Nutr. 46, 593–619. https://doi.org/10.1080/10408390500436185.

Li, S., Chen, J., Xu, W., Sun, B., Wu, J., Chen, Q., Liang, P., 2023. Highly homogeneous bimetallic core–shell Au@Ag nanoparticles with embedded internal standard fabrication using a microreactor for reliable quantitative SERS detection. Mater. Chem. Front. 7, 1100–1109. https://doi.org/10.1039/D2QM01202B.

Li, J., Guan, R., Wuethrich, A., Yan, M., Cheng, J., Liu, G., Zhan, J., Trau, M., Sun, Y., 2024. High accuracy of clinical verification of electrohydrodynamic-driven nanobox-on-mirror platform for molecular identification of respiratory viruses. Anal. Chem. 96, 4495–4504. https://doi.org/10.1021/acs.analchem.3c05120.

Li, Y., Zhang, N., Wang, H., Zhao, Q., 2020. Fluorescence anisotropy-based signal-off and signal-on aptamer assays using lissamine rhodamine b as a label for ochratoxin A. J. Agric. Food Chem. 68, 4277–4283. https://doi.org/10.1021/acs.jafc.0c00549.

Lin, S., Hasi, W., Lin, X., Han, S., Xiang, T., Liang, S., Wang, L., 2020. Lab-on-capillary platform for on-site quantitative sers analysis of surface contaminants based on Au@4-MBA@Ag core–shell nanorods. ACS Sens 5, 1465–1473. https://doi.org/10.1021/acssensors.0c00398.

Lin, S., Kumar Reddy, D.H., Bediako, J.K., Song, M.-H., Wei, W., Kim, J.-A., Yun, Y.-S., 2017. Effective adsorption of Pd(ii), Pt(iv) and Au(iii) by Zr(iv)-based metal–organic frameworks from strongly acidic solutions. J. Phys. Chem. A 5, 13557–13564. https://doi.org/10.1039/C7TA02518A.

Lin, S., Zhao, Y., Bediako, J.K., Cho, C.-W., Sarkar, A.K., Lim, C.R., Yun, Y.-S., 2019. Structure-controlled recovery of palladium(II) from acidic aqueous solution using metal-organic frameworks of MOF-802, UiO-66 and MOF-808. Chem. Eng. J. 362, 280–286. https://doi.org/10.1016/j.cej.2019.01.044.

Liu, M., Wang, J., Yang, Q., Hu, N., Zhang, W., Zhu, W., Wang, R., Suo, Y., Wang, J., 2019. Patulin removal from apple juice using a novel cysteine-functionalized metal-organic framework adsorbent. Food Chem. 270, 1–9. https://doi.org/10.1016/j.foodchem.2018.07.072.

Ma, Y., Li, W., Cho, E.C., Li, Z., Yu, T., Zeng, J., Xie, Z., Xia, Y., 2010. Au@Ag core shell nanocubes with finely tuned and well-controlled sizes, shell thicknesses, and optical properties. ACS Nano 4, 6725–6734. https://doi.org/10.1021/nn102237c.

Ma, H., Pan, S.Q., Wang, W.-L., Yue, X., Xi, X.H., Yan, S., Wu, D.Y., Wang, X., Liu, G., Ren, B., 2024. Surface-enhanced Raman spectroscopy: current understanding, challenges, and opportunities. ACS Nano 18, 14000–14019. https://doi.org/10.1021/acsnano.4c02670.

Mahato, D.K., Kamle, M., Sharma, B., Pandhi, S., Devi, S., Dhawan, K., Selvakumar, R., Mishra, D., Kumar, A., Arora, S., Singh, N.A., Kumar, P., 2021. Patulin in food: a mycotoxin concern for human health and its management strategies. Toxicon 198, 12–23. https://doi.org/10.1016/j.toxicon.2021.04.027.

Martinez, L., He, L., 2020. Detection of mycotoxins in food using surface-enhanced Raman spectroscopy: a review. ACS Appl. Bio Mater. 4, 295–310. https://doi.org/10.1021/acsabm.0c01349.

Mukherjee, M., Appaiah, P., Sistla, S., Bk, B., Bhatt, P., 2022. Bio-layer interferometry-based SELEX and label-free detection of patulin using generated aptamer. J. Agric. Food Chem. 70, 6239–6246. https://doi.org/10.1021/acs.jafc.2c01591.

Olorunyomi, J.F., White, J.F., Gengenbach, T.R., Caruso, R.A., Doherty, C.M., 2022. Fabrication of a reusable carbon dot/gold nanoparticle/metal–organic framework film for fluorescence detection of lead ions in water. ACS Appl. Mater. Interfaces 14, 35755–35768. https://doi.org/10.1021/acsami.2c09122.

Radziuk, D., Grigoriev, D., Zhang, W., Su, D., Möhwald, H., Shchukin, D., 2010. Ultrasound-assisted fusion of preformed gold nanoparticles. J. Phys. Chem. C. 114, 1835–1843. https://doi.org/10.1021/jp910374s.

Ravipati, M., Badhulika, S., 2024. Zr-MOF Nanospheres on Zn-MOF nanorods on ni foam for the electrochemical detection of ivermectin in urine samples. ACS Appl. Nano Mater. 7, 23787–23797. https://doi.org/10.1021/acsanm.4c04237.

Röthlisberger, P., Hollenstein, M., 2018. Aptamer chemistry. Adv. Drug Deliv. Rev. 134, 3–21. https://doi.org/10.1016/j.addr.2018.04.007.

Samuel, H.S., Nweke-Maraizu, U., Etim, E.E., 2024. cyanoacrylate chemistry and polymerization mechanisms. Prog. Chem. Biochem. Res 7, 129–142. https://doi.org/10.48309/pcbr.2024.422869.1304.

Shen, W., Lin, X., Jiang, C., Li, C., Lin, H., Huang, J., Wang, S., Liu, G., Yan, X., Zhong, Q., Ren, B., 2015. Reliable quantitative SERS analysis facilitated by core–shell nanoparticles with embedded internal standards. Angew. Chem. Int. Ed. 54, 7308–7312. https://doi.org/10.1002/anie.201502171.

Sun, J., Li, W., Zhu, X., Jiao, S., Chang, Y., Wang, S., Dai, S., Xu, R., Dou, M., Li, Q., Li, J., 2021. A novel multiplex mycotoxin surface-enhanced Raman spectroscopy immunoassay using functional gold nanotags on a silica photonic crystal

microsphere biochip. J. Agric. Food Chem. 69, 11494–11501. https://doi.org/10.1021/acs.jafc.1c03469.
Wang, S., McGuirk, C.M., Ross, M.B., Wang, S., Chen, P., Xing, H., Liu, Y., Mirkin, C.A., 2017. General and direct method for preparing oligonucleotide-functionalized metal–organic framework nanoparticles. J. Am. Chem. Soc. 139, 9827–9830. https://doi.org/10.1021/jacs.7b05633.
Wang, P.L., Xie, L.H., Joseph, E.A., Li, J.R., Su, X.O., Zhou, H.C., 2019. Metal–organic frameworks for food safety. Chem. Rev. 119, 10638–10690. https://doi.org/10.1021/acs.chemrev.9b00257.
Wang, Y., Yan, B., Chen, L., 2012. SERS tags: novel optical nanoprobes for bioanalysis. Chem. Rev. 113, 1391–1428. https://doi.org/10.1021/cr300120g.
Wei, C., Yu, L., Qiao, N., Zhao, J., Zhang, H., Zhai, Q., Tian, F., Chen, W., 2020. Progress in the distribution, toxicity, control, and detoxification of patulin: a review. Toxicon 184, 83–93. https://doi.org/10.1016/j.toxicon.2020.05.006.
Wu, Z., Pu, H., Sun, D.-W., 2021. Fingerprinting and tagging detection of mycotoxins in agri-food products by surface-enhanced Raman spectroscopy: principles and recent applications. Trends Food Sci. Technol. 110, 393–404. https://doi.org/10.1016/j.tifs.2021.02.013.
Xiang, Y., Yan, H., Zheng, B., Faheem, A., Hu, Y., 2020. Microorganism@UiO-66-NH_2 composites for the detection of multiple colorectal cancer-related micrornas with flow cytometry. Anal. Chem. 92, 12338–12346. https://doi.org/10.1021/acs.analchem.0c02017.
Xing, K.Y., Peng, J., Shan, S., Liu, D.F., Huang, Y.N., Lai, W.H., 2020. Green enzyme-linked immunosorbent assay based on the single-stranded binding protein-assisted aptamer for the detection of mycotoxin. Anal. Chem. 92, 8422–8426. https://doi.org/10.1021/acs.analchem.0c01073.
Xu, M.L., Gao, Y., Han, X.X., Zhao, B., 2017. Detection of pesticide residues in food using surface-enhanced raman spectroscopy: a review. J. Agric. Food Chem. 65, 6719–6726. https://doi.org/10.1021/acs.jafc.7b02504.
Xue, S., Yin, L., Gao, S., Zhou, R., Zhang, Y., Jayan, H., El-Seedi, H.R., Zou, X., Guo, Z., 2024. A film-like SERS aptasensor for sensitive detection of patulin based on GO@Au nanosheets. Article e138364 Food Chem. 441. https://doi.org/10.1016/j.foodchem.2024.138364.
Yang, J., Li, W., Li, H., Wang, X., Xu, K., Li, Q., Zheng, T., Li, J., 2024. Highly sensitive microarray immunoassay for multiple mycotoxins on engineered 3D porous silicon SERS substrate with silver nanoparticle magnetron sputtering. Anal. Chem. 96, 2425–2434. https://doi.org/10.1021/acs.analchem.3c04359.
Yin, L., Cai, J., Ma, L., You, T., Arslan, M., Jayan, H., Zou, X., Gong, Y., 2024. Dual function of magnetic nanocomposites-based SERS lateral flow strip for simultaneous detection of aflatoxin B1 and zearalenone. Food Chemistry 446, 138817. https://doi.org/10.1016/j.foodchem.2024.138817.
Zhang, K., Xi, Z., Wu, Z., Lu, G., Huang, X., 2021. Visible-light-induced selective oxidation of amines into imines over UiO-66-NH2@Au@COF core–shell photocatalysts. ACS Sustain. Chem. Eng. 9, 12623–12633. https://doi.org/10.1021/acssuschemeng.1c04112.
Zhang, H., Yang, S., De Ruyck, K., Beloglazova, N., Eremin, S.A., de Saeger, S., Zhang, S., Shen, J., Wang, Z., 2019. Fluorescence polarization assays for chemical contaminants in food and environmental analyses. Trends Anal. Chem. 114, 293–313. https://doi.org/10.1016/j.trac.2019.03.013.
Zhang, Z., Zhang, Y., Jayan, H., Gao, S., Zhou, R., Yosri, N., Guo, Z., 2024. Recent and emerging trends of metal-organic frameworks (MOFs)-based sensors for detecting food contaminants: A critical and comprehensive review. Food Chemistry 448, 139051. https://doi.org/10.1016/j.foodchem.2024.139051.
Zhao, Q., Tao, J., Uppal, J.S., Peng, H., Wang, H., Le, X., 2019. Nucleic acid aptamers improving fluorescence anisotropy and fluorescence polarization assays for small molecules. Trends Anal. Chem. 110, 401–409. https://doi.org/10.1016/j.trac.2018.11.018.
Zhou, H.-C., Long, J.R., Yaghi, O.M., 2012. Introduction to metal–organic frameworks. Chem. Rev. 112, 673–674. https://doi.org/10.1021/cr300014x.